Human Molecular Genetics, 2022, Vol. 00, 00, 1–13
https://doi.org/10.1093/hmg/ddac071
Advance access publication date 26 March 2022
Original Article

Expanding the molecular spectrum of pathogenic *SHOC2* variants underlying Mazzanti syndrome

Marialetizia Motta[1,†], Maja Solman[2,†], Adeline A. Bonnard[3,4,‡], Alma Kuechler[5,‡], Francesca Pantaleoni[1,‡], Manuela Priolo[6,‡], Balasubramanian Chandramouli[7], Simona Coppola[8], Simone Pizzi[1], Erika Zara[1,9], Marco Ferilli[1], Hülya Kayserili[10], Roberta Onesimo[11], Chiara Leoni[11], Julia Brinkmann[12], Yoann Vial[3,4], Susanne B. Kamphausen[12], Cécile Thomas-Teinturier[13,14], Anne Guimier[15], Viviana Cordeddu[16], Laura Mazzanti[17], Giuseppe Zampino[11,18], Giovanni Chillemi[19,20], Martin Zenker[5,¶], Hélène Cavé[3,4,¶], Jeroen den Hertog[2,¶] and Marco Tartaglia[1,¶,*]

[1]Genetics and Rare Diseases Research Division, Ospedale Pediatrico Bambino Gesù, IRCCS, 00146 Rome, Italy
[2]Hubrecht Institute-KNAW and University Medical Center Utrecht, 3584 Utrecht, The Netherlands
[3]Département de Génétique, Assistance Publique des Hôpitaux de Paris (AP-HP), Hôpital Robert Debré, 75019 Paris, France
[4]INSERM UMR 1131, Institut de Recherche Saint-Louis, Université de Paris, 75010 Paris, France
[5]Institut für Humangenetik, Universitätsklinikum Essen, Universität Duisburg-Essen, 45147 Essen, Germany
[6]UOSD Genetica Medica, Grandeospedale Metropolitano "Bianchi-Melacrino-Morelli", 89124 Reggio Calabria, Italia
[7]Super Computing Applications and Innovation, CINECA, 40033 Bologna, Italy
[8]National Centre Rare Diseases, Istituto Superiore di Sanità, 00161 Rome, Italy
[9]Department of Biology and Biotechnology "Charles Darwin", Sapienza University of Rome, 00185 Rome, Italy
[10]Genetic Diseases Evaluation Center, Medical Genetics Department, KoçUniversity School of Medicine, İstanbul 34010, Turkey
[11]Center for Rare Diseases and Birth Defects, Department of Woman and Child Health and Public Health, Fondazione Policlinico Universitario A. Gemelli, IRCCS, 00168 Rome, Italy
[12]Institute of Human Genetics, University Hospital Magdeburg, 39120 Magdeburg, Germany
[13]Department of Pediatric Endocrinology, Assistance Publique-Hôpitaux de Paris, Université Paris-Saclay, Hôpital Bicêtre, 94270 Le Kremlin Bicêtre, France
[14]INSERM UMR 1018, Cancer and Radiation Team, CESP, 94800 Villejuif, France
[15]Service de Médecine Genomique des Maladies Rares, CRMR Anomalies du développement, Hôpital Necker-Enfants Malades, Assistance Publique des Hôpitaux de Paris, 75015 Paris, France
[16]Department of Oncology and Molecular Medicine, Istituto Superiore di Sanità, 00161 Rome, Italy
[17]Alma Mater Studiorum, University of Bologna, 40125 Bologna, Italy
[18]Department of Woman and Child Health and Public Health, Università Cattolica del Sacro Cuore, 00168 Rome, Italy
[19]Department for Innovation in Biological, Agro-food and Forest systems, Università della Tuscia, 01100 Viterbo, Italy
[20]Istituto di Biomembrane, Bioenergetica e Biotecnologie Molecolari, Centro Nazionale delle Ricerche, 70126 Bari, Italy
*To whom correspondence should be addressed at: Genetics and Rare Diseases Research Division, Ospedale Pediatrico Bambino Gesù, 00146 Rome, Italy. Tel: +39 0668593742; Email: marco.tartaglia@opbg.net

[†]These co-first authorship equally contributed to this work.

[‡]These "second position" authorship equally contributed to this work.

[¶]These authors jointly coordinated this work.

Abstract

We previously molecularly and clinically characterized Mazzanti syndrome, a RASopathy related to Noonan syndrome that is mostly caused by a single recurrent missense variant (c.4A > G, p.Ser2Gly) in *SHOC2*, which encodes a leucine-rich repeat-containing protein facilitating signal flow through the RAS-mitogen-associated protein kinase (MAPK) pathway. We also documented that the pathogenic p.Ser2Gly substitution causes upregulation of MAPK signaling and constitutive targeting of SHOC2 to the plasma membrane due to the introduction of an *N*-myristoylation recognition motif. The almost invariant occurrence of the pathogenic c.4A > G missense change in *SHOC2* is mirrored by a relatively homogeneous clinical phenotype of Mazzanti syndrome. Here, we provide new data on the clinical spectrum and molecular diversity of this disorder and functionally characterize new pathogenic variants. The clinical phenotype of six unrelated individuals carrying novel disease-causing *SHOC2* variants is delineated, and public and newly collected clinical data are utilized to profile the disorder. *In silico*, *in vitro* and *in vivo* characterization of the newly identified variants provides evidence that the consequences of these missense changes on SHOC2 functional behavior differ from what had been observed for the canonical p.Ser2Gly change but converge toward an enhanced activation of the RAS-MAPK pathway. Our findings expand the molecular spectrum of pathogenic *SHOC2* variants, provide a more accurate picture of the phenotypic expression associated with variants in this gene and definitively establish a gain-of-function behavior as the mechanism of disease.

Received: February 23, 2022. **Revised:** March 15, 2022. **Accepted:** March 18, 2022
© The Author(s) 2022. Published by Oxford University Press. All rights reserved. For Permissions, please email: journals.permissions@oup.com
This is an Open Access article distributed under the terms of the Creative Commons Attribution-NonCommercial License (http://creativecommons.org/licenses/by-nc/4.0/), which permits non-commercial re-use, distribution, and reproduction in any medium, provided the original work is properly cited. For commercial re-use, please contact journals.permissions@oup.com

Downloaded from https://academic.oup.com/hmg/advance-article/doi/10.1093/hmg/ddac071/6553889 by Koc University user on 27 April 2022

Introduction

Mazzanti syndrome, also known as Noonan syndrome-like with loose anagen hair (MIM: 607721, 617506), is an autosomal dominantly transmitted RASopathy characterized by features resembling Noonan syndrome (NS; MIM: PS163950). The typical facies includes relative macrocephaly, hypertelorism, ptosis, downslanted palpebral fissures and low-set posteriorly rotated ears (1). Similar to NS, affected individuals also show postnatally reduced growth, which is commonly associated with growth hormone deficiency (GHD), cardiac defects, particularly dysplasia of the mitral valve, webbed neck, pectus defects, cognitive deficits and behavioral anomalies (1,2). Distinctive features include ectodermal anomalies, the most characteristic sign being easily pluckable, sparse, thin, slow-growing hair (loose anagen hair), a hyperpigmented skin and a hypernasal voice (1,2).

The majority of patients with Mazzanti syndrome share a recurrent missense change in *SHOC2* (c.4A > G, p.Ser2Gly; NM_001324336.2) (2), which encodes a leucine-rich repeat (LRR)-containing protein facilitating signal flow through the RAS-mitogen-associated protein kinase (MAPK) pathway in response to growth factors and other stimuli (3,4). More recently, a narrow spectrum of missense variants in *PPP1CB*, encoding one of the three catalytic subunits of protein phosphatase 1 (PP1), was identified to underlie this disorder in a small proportion of patients (5,6). Notably, SHOC2 functions as a PP1 regulatory subunit promoting translocation of the catalytic subunit to the plasma membrane (3), which is required for the dephosphorylation of the inhibitory Ser^{259} of RAF1 and activation of the kinase (7). SHOC2 translocation to the plasma membrane is attained by binding to MRAS, a GTPase belonging to the RAS family that is also mutated in NS (8,9). We previously showed that the pathogenic p.Ser2Gly substitution causes constitutive targeting of SHOC2 to the plasma membrane due to the introduction of an *N*-myristoylation recognition motif that promotes a stable membrane-bound status of the mutant and upregulation of MAPK signaling (2).

The almost invariant occurrence of the c.4A > G missense change in *SHOC2* is mirrored by a relatively homogeneous clinical phenotype of Mazzanti syndrome (2,10). Recently, two different pathogenic variants of *SHOC2*, c.519G > A (p.Met173Ile) and c.807_808delinsTT (p.Gln269_His270delinsHisTyr), were reported in two individuals with milder phenotypes partially overlapping NS and cardiofaciocutaneous syndrome (MIM: PS115150), and a severe condition characterized by prenatal-onset hypertrophic cardiomyopathy, respectively (11,12). There are conflicting data regarding the consequences of these pathogenic *SHOC2* variants on protein function and MAPK signaling. While p.Met173Ile was originally proposed to cause loss of function (LoF) (11), we and others provided evidence supporting the activating role of the two *SHOC2* variants in terms of protein binding to MRAS and PPP1CB, enhanced/stabilized ternary complex formation and overall increased signaling through the MAPK cascade (2,7,12,13).

Here we report on the identification and functional validation of novel pathogenic *SHOC2* variants and delineate the associated clinical phenotype. Our findings expand the molecular diversity of pathogenic *SHOC2* mutations, confirm their gain-of-function (GoF) role in the context of MAPK signaling and provide a more accurate profiling of the clinical spectrum resulting from mutated *SHOC2* alleles.

Results

Genetic and clinical findings

In six individuals clinically diagnosed with Mazzanti syndrome, NS or having a clinically related phenotype, missense variants in *SHOC2* affecting conserved residues among orthologs within regions variably intolerant for variation were identified (Table 1, Supplementary Material, Figs S1 and S2). Four of them had not previously been reported in public databases; c.517A > G (p.Met173Val) had been annotated as likely pathogenic in ClinVar (VCV000373090). One variant (p.Gln269Arg) was identified in two unrelated individuals (1 and 4); similarly, one residue, Met^{173}, was mutated in two subjects (2 and 5). Both p.Met173Val and p.Gln269Arg affected residues previously reported as mutated by different substitutions in individuals with features within the RASopathy phenotypic spectrum (11,12). Segregation analysis confirmed their *de novo* origin in all families. However, *in silico* tools predicted a putative damaging impact only for two of them, and all variants but c.517A > G were classified as VoUS according to the ACMG criteria (Table 1).

A homogenous presentation for facial features, ectodermal involvement and other features reported in Mazzanti syndrome was evinced among individuals (Fig. 1A, Supplementary Material, Table S1), in absence of any obvious genotype–phenotype correlation. The clinical profile of the six subjects is summarized in Table 1, and their detailed clinical history and facial features are provided in the supplemental section (**Clinical Reports**). Overall, these subjects shared facial features resembling NS (6/6), relative macrocephaly (6/6) and typical scalp and cutaneous ectodermal abnormalities occurring in Mazzanti syndrome (5/6). In subjects 1 and 2, trichorrhexis nodosa, a sign previously reported in Mazzanti syndrome (14), was documented (Supplementary Material, Fig. S3). Subject 1 also had a hypernasal voice, a feature previously described in Mazzanti syndrome. Mild motor delay was observed in five individuals, and associated with speech delay (3/5) or attention deficit (1/5). Subjects 1 and 6 were reported to have normal cognitive development. Skeletal involvement (pectus excavatum, most commonly) was reported in four subjects, while short stature (<3rd centile) in two individuals, both diagnosed with GHD. One

Downloaded from https://academic.oup.com/hmg/advance-article/doi/10.1093/hmg/ddac071/6553889 by Koc University user on 27 April 2022

Table 1. Clinical findings in individuals with novel pathogenic *SHOC2* variants

Subject	1	2	3	4	5	6
Gender	male	female	male	male	female	male
Ethnicity	Turkish	German	French	French	French	Italian
NT change AA change	c.806A > G p.Gln269Arg	c.517A > G p.Met173Val	c.1231A > G p.Thr411Ala	c.806A > G p.Gln269Arg	c.519_520delinsAT p.Met173_Leu174 delinsIlePhe	c.157G > A p.Gly53Arg
CADD score*	24.7	9.29	25.7	24.7	18.5	25.0
M-CAP score*	0.102	0.099	0.025	0.102	NA	0.084
REVEL score*	0.531	0.428	0.289	0.531	NA	0.518
ACMG class*	VoUS PM2, PM6	likely pathogenic PM2, PM5, PM6, PP5	VoUS PM2, PM6	VoUS PM2, PM6	VoUS PM2, PM6	VoUS PM2, PM6
Segregation	*de novo*	*de novo*	*de novo*	*de novo*	*de novo*	*de novo*
Prenatal findings	none	none	NA	none	nuchal edema (4.7 mm)	none
Gestat. age	38 weeks	37 weeks	40 weeks	40 weeks	39 weeks	38 weeks
weight [SD]	4000 g [1.36]	3300 g [0.7]	4580 g [3.17]	2370 g [−2.71]	3660 g [1.18]	2800 g [− 0.99]
length [SD]	52 cm [0.91]	50 cm [0.2]	53 cm [1.5]	47 cm [−2.02]	49 cm [−0.67]	48 cm [−0.8]
OFC [SD]	NA	33 cm [−0.6]	36 cm [1.12]	34 cm [−0.66]	35 cm [0.96]	35 cm [0.69]
Feeding difficulties	none	poor feeder in infancy	none	poor feeder	poor feeder, required tube feeding	none
Mazzanti syndrome facial gestalt	suggestive	typical	suggestive	suggestive	suggestive	suggestive
sparse eyebrows	+	+	+	+	+	+
Short/broad neck	yes	none	yes	yes	yes	yes
Hair and skin features	sparse slow-growing hair (frontotemporal regions), hairy nevus (upper leg), deep palmar/plantar creases, trichorrhexis nodosa	sparse loose hair, diffuse skin hyperpigmentation, trichorrhexis nodosa	curly hair, multiple nevi	brittle hair, eczema, dry skin	sparse fine slow-growing hair, ichthyosis, diffuse skin hyperpigmentation, 1 café-au-lait spot	sparse hair, palmar/plantar hyperxerosis
Lymphatic anomalies	none	none	NA	none	none	none
Height [SD]	110.5 cm [−1.48]	97.7 cm [−2.2]	177 cm [−0.23]	82 cm [−1.8]	77 cm [−1.57]	136 cm [−0.92]
Weight [SD]	17.5 kg [−1.51]	15.8 kg [−0.9]	59 kg [−0.58]	10 kg [−2.5]	9.9 kg [−1.37]	29.4 Kg [−1.9]
OFC [SD]	53.5 cm [+1.13]	52 cm [+1.3]	58 cm [+0.7]	49 cm [−0.7]	48 cm [0.84]	54.5 cm [+ 1]
(age)	6 y 3 m	4 y 7 m	17 y 11 m	2 y 6 m	1 y 8 m	10 y 9 m
GHD	yes, neurosecretory dysfunction	yes, neurosecretory dysfunction; GH treatment started at age 3y 5 m (height SD prior to treatment: −2.5; now 3rd–10th percentile)	no	yes	no	no
Developmental abnormalities	mild motor delay, normal speech and cognitive development, short attention span	mild motor and speech delay, learning disability (IQ 75)	mild motor and significant speech delay, moderate Intellectual disability (IQ 49)	mild motor and speech delay	mild motor delay	no intellectual disability or motor delay (IQ 131)
Neurologic features	muscular axial hypotonia, minimal extracerebral prominence, epileptic seizure (once)	none	epilepsy (in treatment)	none	none	Chiari malformation, type 1
Ocular abnormalities	none	none	strabismus, ptosis	ptosis	strabismus, ptosis	ptosis
Hearing deficit	none	none	yes, sensorineural	none	none	none
Heart abnormalities	bicuspid aortic valve	none	left bundle branch block	none	atrial septal defect	bicuspid aortic valve, aortic bulb ectasia
Skeletal abnormalities	ulnar deviation at wrists, cubitus valgus, mild hyperextensibility of MCP-PIP joints, delayed bone age	delayed closure of the large fontanel, delayed bone age	mild pectus excavatum	pectus excavatum	none	pectus excavatum
Genito-urinary anomalies	retractile testis (unilateral), shawl scrotum	NA	hydronephrosis due to ureteral stenosis/reflux requiring surgical treatment, cryptorchidism	none	none	retractile testis
Additional	left accessory nipple, hypernasal voice, recurrent infections	none	none	none	constipation	autoimmune thyroiditis

GH, growth hormone; GHD, growth hormone deficiency; m, months; NA, not available; NS, Noonan syndrome; NSLH; Noonan syndrome-like with loose anagen hair; y, years. ClinVar IDs: SCV002073494 (c.157G > A, p.Gly53Arg); SCV002073493 (c.517A > G, p.Met173Val); SCV002073718 (c.519_520delinsAT, p.Met173_Leu174delinsIlePhe); SCV002073492 and SCV002073716 (c.806A > G, p.Gln269Arg); SCV001438562 (c.1231A > G, p.Thr411Ala). *Pathogenicity thresholds: CADD > 15, M-CAP > 0.025, REVEL > 0.5. ACMG classification has been assessed using VarSome (https://varsome.com/).

Downloaded from https://academic.oup.com/hmg/advance-article/doi/10.1093/hmg/ddac071/6553889 by Koc University user on 27 April 2022

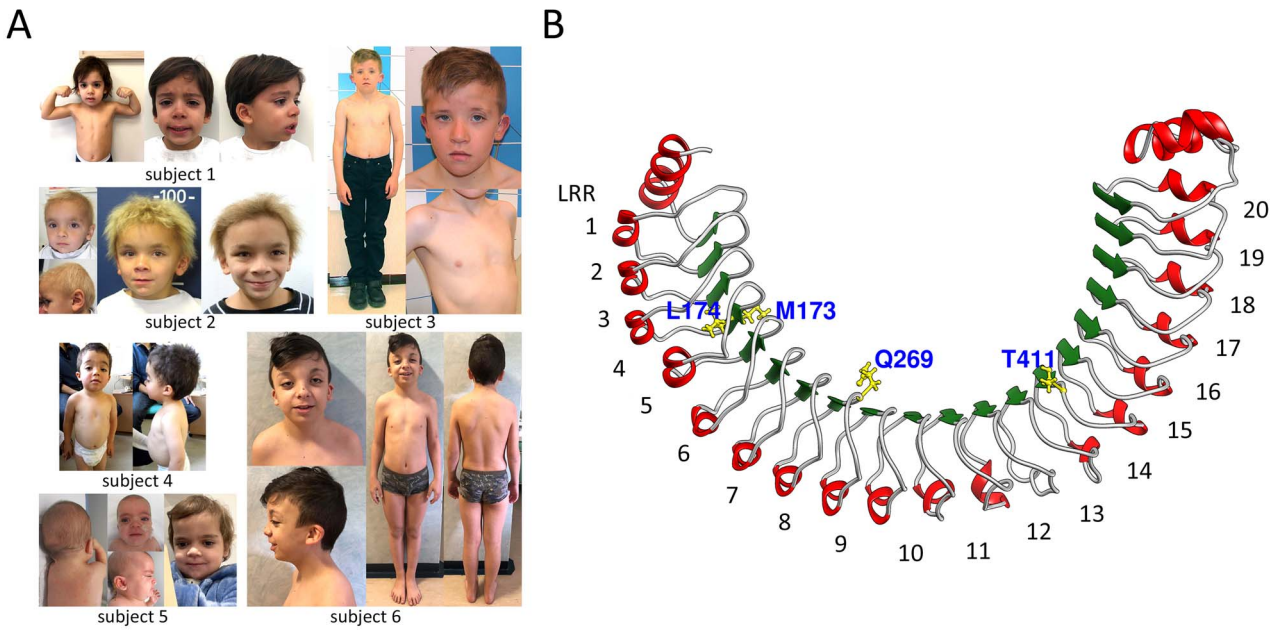


Figure 1. Clinical features of the six subjects with novel pathogenic variants in *SHOC2*, and location of the amino acid substitutions. (**A**) Clinical features of the six reported individuals. Note the facial *gestalt* (downslanted palpebral fissures, hypertelorism, ptosis, bushy lateral sparse eyebrows, low-set ears with fleshy upturned earlobe, long philtrum and exaggerated Cupid bow), distinctive hair anomalies, pectus excavatum, short and webbed neck and low posterior hairline. (**B**) 3D model of the SHOC2's LRR domain. Residues 85–582 are shown in cartoon representation. α-Helices and β-strands are in red and green colors, respectively. The side chains of affected residues are highlighted in yellow. Numbering of LRRs is also reported. Each LRR is composed by a conserved region having a β-strand fold and a variable one, usually structured as α-helix. Note that all mutated residues fall within the conserved β-strand region of LRRs that form the horseshoe shaped parallel β-sheet.

individual started growth hormone replacement therapy, which resulted in increased growth velocity. Cardiac defects occurred in four individuals, none presenting right side involvement. Two subjects presented with bicuspid aortic valve, which was associated with mild aortic bulb ectasia in one, while atrial septal defect and left bundle branch block were observed in single subjects. No lymphatic anomalies were reported. Cryptorchidism/retractile testis occurred in three of four male individuals. Two subjects experienced epileptic episodes, and one showed Chiari malformation 1.

Detailed assessment of facial features revealed a distinctive and homogeneous craniofacial appearance including high forehead (6/6), bitemporal narrowing (5/6), hypertelorism (5/6), long downslanted palpebral fissures (6/6), ptosis (4/6), short triangular nose with anteverted nares (6/6), broad and deep philtrum (6/6), exaggerated cupid bow (5/6) and low-set posteriorly rotated ears with prominent folded helix (6/6) (Supplementary Material, Table S1). A short/broad neck (5/6) with low posterior hairline (4/6) was also a commonly shared feature. Most of these signs are frequent features in NS and other RASopathies (Human Phenotype Ontology database, https://hpo.jax.org/app/browse/disease/ORPHA:648). Of note, sparse lateral eyebrows were documented in all subjects (6/6), indicating this previously unappreciated ectodermal sign as a facial hallmark of Mazzanti syndrome. To compare the facial profile of these subjects with that of individuals with the recurrent c.4A > G change (p.Ser2Gly), the previously reported clinical pictures of 30 subjects were reviewed by 4 experienced clinical geneticists (L.M., M.P., G.Z. and M.Z.), and the relative prevalence of each sign/feature was compared (Supplementary Material, Table S1). No preferential association was observed. Then, the prevalence of the same signs/features was compared considering the entire *SHOC2* cohort and the group of 15 subjects carrying pathogenic variants in *PPP1CB* who had published pictures, documenting an overlap in frequency, with exceptions being deep philtrum and upper lip conformation (i.e. exaggerated cupid bow), which were less frequent in the *PPP1CB* cohort, and bitemporal narrowing, less frequently reported in the *SHOC2* cohort (Supplementary Material, Table S1). Overall, the phenotypic assessment provided evidence of a relatively homogeneous presentation and a recognizable facies.

Structural and biochemical characterization of the identified *SHOC2* variants

SHOC2 is composed of an unstructured N-terminal region (residues 2–101) followed by a domain of 20 tandemly arranged LRR motifs (residues 102–564) (15), the latter organized in a horseshoe shape fold with a parallel β-sheet on the concave face mediating SHOC2's binding to signaling partners (Fig. 1B) (16). Based on the generated 3D model, Met^{173} and Leu^{174} (LRR4), Gln^{269} (LRR8) and Thr^{411} (LRR14) were found to map within the β-strand folds of individual LRRs forming the β-sheet of the concave face and were solvent-exposed with side chains projecting outward. We performed MD simulations using the *ab initio* AlphaFold model to further explore their structural impact. All structures

Downloaded from https://academic.oup.com/hmg/advance-article/doi/10.1093/hmg/ddac071/6553889 by Koc University user on 27 April 2022

were stable over the simulation time window, rejecting a major disruptive effect of the introduced substitutions (Supplementary Material, Figs S4 and S5). Consistently, the secondary structure was well conserved within the LRR domains of all simulated systems (Supplementary Material, Fig. S6), and local inspection of the three affected LRRs confirmed that no major local perturbation was introduced by the amino acid changes (Supplementary Material, Figs S7 and S8, Table S3). In line with these findings, no substantial structural rearrangement was observed in the MD simulation of the protein carrying the previously identified bona fide pathogenic p.Met173Ile. Taken together, the collected *in silico* data did not provide any evidence of drastic structural rearrangements promoted by the variants. Based on their clustering within the LRRs' β-strands, a possible effect on the β-sheet in terms of intermolecular interactions with signaling partners was hypothesized.

To validate the *in silico* analyses, COS-1 cells were transiently transfected to express the wild-type (WT) protein ($SHOC2^{WT}$), the recurrent Mazzanti syndrome-causing $SHOC2^{S2G}$ or each of the five generated mutants ($SHOC2^{G53R}$, $SHOC2^{M173V}$, $SHOC2^{Q269R}$, $SHOC2^{T411A}$ and $SHOC2^{M173_L174delinsIF}$), and their stability was first analyzed. Following immunoblotting, quantitative analyses documented that the protein levels of mutants were similar to those characterizing $SHOC2^{WT}$, basally, and following cycloheximide (CHX) or MG132 treatment (Fig. 2A), indicating that all the tested substitutions do not affect significantly the stability of the protein.

In vitro functional characterization studies

We previously demonstrated that p.Ser2Gly substitution promotes SHOC2 constitutive targeting to the plasma membrane (2). Differently from the canonical $SHOC2^{S2G}$ mutant, $SHOC2^{WT}$ is uniformly distributed in the cytoplasm and nucleus under serum-starved condition, and translocates to the nucleus following stimulation with epidermal growth factor (EGF), indicating that the protein has only a brief, rapidly reversed localization at the plasma membrane (2). The subcellular distribution of the SHOC2 mutants was investigated by confocal laser scanning microscopy in serum-starved and EGF-stimulated transfected COS-1 cells (Fig. 2B). None of the mutants displayed constitutive targeting to the plasma membrane. Each mutant was distributed in both cytoplasm and nucleus during starvation and translocated to the nucleus following stimulation with EGF, similar to what was observed for the $SHOC2^{WT}$. This subcellular distribution pattern was confirmed by cell fractionation experiments (Fig. 2C).

We previously showed that the pathogenic $SHOC2^{S2G}$ protein promotes enhanced signaling through the MAPK cascade (2). To verify the presence of signal dysregulation through this pathway, we analyzed the levels of ERK phosphorylation associated with transient overexpression of $SHOC2^{WT}$ and each of the SHOC2 mutants in Neuro2A cells (Fig. 3A), a line for which the capability of SHOC2 to modulate ERK signaling had previously been demonstrated (2,15). As expected, $SHOC2^{S2G}$ expression promoted boosted and sustained EGF-dependent ERK phosphorylation compared to what was observed in cells expressing the WT protein. A statistically significant variably enhanced ERK activation was also documented for all mutants, providing evidence for their activating role on MAPK signaling.

The positive modulatory role of SHOC2 on RAS-MAPK signaling has been linked to the function of the protein to interact with GTP-bound MRAS and promote PP1C translocation to the plasma membrane (3,7,17,18). To explore the possibility that mutations promote a more stable/enhanced binding of SHOC2 to MRAS and/or PPP1CB, co-IP experiments were performed using cell lysates collected from Neuro2A cells transiently co-expressing V5-tagged WT or mutant SHOC2 proteins with Myc-tagged MRAS or Myc-tagged PPP1CB (Fig. 3B). As shown, all SHOC2 mutants displayed an increased binding to both MRAS and PPP1CB, compared with what was observed for $SHOC2^{WT}$, correlating with their improved ability to activate the MAPK pathway.

Overall, the collected *in vitro* data provide evidence that the newly identified RASopathy-associated *SHOC2* variants are activating and enhance signaling through the MAPK cascade. This effect is associated with an increased and/or more stable binding of SHOC2 to both MRAS and PP1C, though apparently does not result from a constitutive targeting of these proteins to the plasma membrane, at least in the used experimental conditions.

Expression of pathogenic *SHOC2* variants in zebrafish induce RASopathy-associated developmental defects *in vivo*

CRISPR/Cas9-mediated knock-out of *Shoc2* induces severe defects in zebrafish embryonic development, particularly in neural crest and hematopoietic lineages, and is lethal in early larval stages (19), indicating an important role of Shoc2 in zebrafish development. Based on these findings, we performed an *in vivo* functional characterization of the identified *SHOC2* variants using zebrafish as an *in vivo* model system. The amino acid substitutions corresponding to the p.Ser2Gly, p.Gly53Arg, p.Met173Ile, p.Met173Val and p.Thr411Ala substitutions were introduced in the zebrafish *Shoc2* cDNA (Supplementary Material, Fig. S2), and the disease-causing alleles were expressed in embryos by mRNA microinjection at the one-cell stage. Embryos expressing WT or mutant Shoc2 proteins were then examined to assess the effects of these mutants on development. Previous studies demonstrated that ectopic induction of MAPK signaling induces defective convergence and extension cell movements during gastrulation and, as a result, embryos are oval in shape, at the 3 somite stage (i.e. 11 h post fertilization, hpf) (20,21). We measured the major-to-minor axis ratio of the injected embryos at 11 hpf. The non-injected and WT *Shoc2*-injected embryos showed an almost perfect spherical shape, whereas

Downloaded from https://academic.oup.com/hmg/advance-article/doi/10.1093/hmg/ddac071/6553889 by Koc University user on 27 April 2022

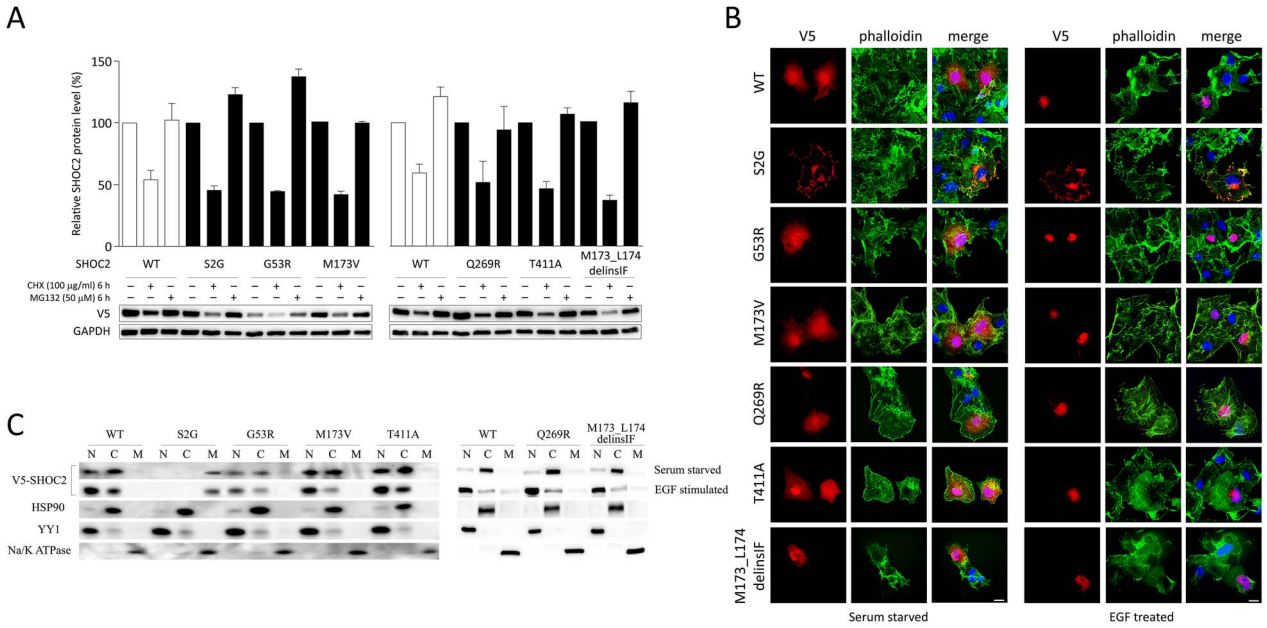


Figure 2. Stability and subcellular localization of the SHOC2 proteins carrying each of the identified pathogenic variants causing Mazzanti syndrome. (**A**) Western blotting analysis showing WT and mutant V5-tagged SHOC2 protein levels in transfected COS-1 cells, basally and after CHX (100 μg/ml) or MG132 (50 μM) treatment. Representative blots (below) and mean ± SD densitometry values (above) of three independent experiments are shown. GAPDH was used as loading control. (**B**) Subcellular localization of the generated V5-tagged SHOC2 mutants assessed by confocal microscopy analysis**.** Localization of the transiently expressed mutants in COS-1 cells during starvation or following EGF stimulation (15 min). Cells were stained with a mouse anti-V5 monoclonal antibody and Alexa Fluor 594 goat anti-mouse secondary antibody (red). Alexa Fluor 488 phalloidin dye (green) was used to stain the f-actin to delineate the cortical actin associated with the plasma membrane. Nuclei are DAPI stained (blue). Merged images are shown in the right panels. Scale bar, 10 μM. (**C**) Localization of the overexpressed mutant proteins in COS-1 cells cultured in serum-starved or EGF-treated conditions determined by cell fractionation experiments. Three fractions were resolved: nucleus (N), cytoplasm (C) and plasma membrane (M). SHOC2 mutants were visualized using an anti-V5 antibody. Antibodies directed to recognize YY1 (nucleus), HSP90 (cytoplasm) and Na/K-ATPase (plasma membrane) were used to assess proper fractioning of the cell lysates.

embryos injected with the RASopathy-associated *Shoc2* mutants appeared oval-shaped (Fig. 4A). The major-to-minor axis ratio was significantly increased in all embryos expressing the pathogenic variants, compared to what was observed in WT *Shoc2*-injected embryos, with the strongest effect observed for the p.Ser2Gly variant.

We assessed the morphological changes in injected embryos at 3 and 5 days post fertilization (dpf). Expression of all disease-causing Shoc2 mutants induced phenotypes in zebrafish embryos that range from mildly to severely disorganized development. Most of the injected embryos appeared shorter in size and displayed heart edemas, enlarged yolk and craniofacial defects, such as smaller eyes, protrusion of the lower jaw and reduction in forebrain structures anterior to the eyes. Overexpression of WT Shoc2 did not affect the morphology of embryos. We quantified the effect of the *Shoc2* variants on embryonic growth by measuring the body axis length, which was significantly reduced in embryos expressing each of the disease-causing Shoc2 mutants at 3 and 5 dpf (Fig. 4B and Supplementary Material, Fig. S9).

We previously showed that ectopic expression of NS-causing *Shp2* variants induces defective early cardiac development, resulting in aberrant cardiac looping (22). To explore whether expression of Mazzanti syndrome-associated *SHOC2* variants induces similar defects, we performed *in situ* hybridization on zebrafish embryos at 3 dpf, using the *myl7*-specific probe, which stains cardiomyocytes (Fig. 4C). Proper heart looping was observed in embryos injected with WT *Shoc2*, while defective heart looping was documented in a significant proportion of embryos injected with the pathogenic *Shoc2* variants, with the strongest effect observed in embryos expressing p.M152I (p.Thr411Ala in SHOC2) (42% of embryos).

Finally, features of craniofacial development were characterized by Alcian blue staining of the cartilage of the injected embryos at 4 dpf. Embryos expressing each of the Shoc2 mutants consistently induced narrowing of the ceratohyal angle compared to non-injected embryos or WT *Shoc2*-injected embryos (Fig. 4D). We quantified the craniofacial defects by measuring the ratio of the width of the ceratohyal (x) and the distance to Meckel's cartilage (y). All mutants induced a significant decrease in the ratio, compared with what was observed in the WT *Shoc2*-injected embryos.

Overall, the developmental defects in zebrafish embryos expressing the pathogenic SHOC2 mutants did not resemble those in embryos lacking functional Shoc2 (19), in line with the GoF behavior of these mutants. On the contrary, they were reminiscent of those induced by NS-associated variants during gastrulation (convergence

Downloaded from https://academic.oup.com/hmg/advance-article/doi/10.1093/hmg/ddac071/6553889 by Koc University user on 27 April 2022

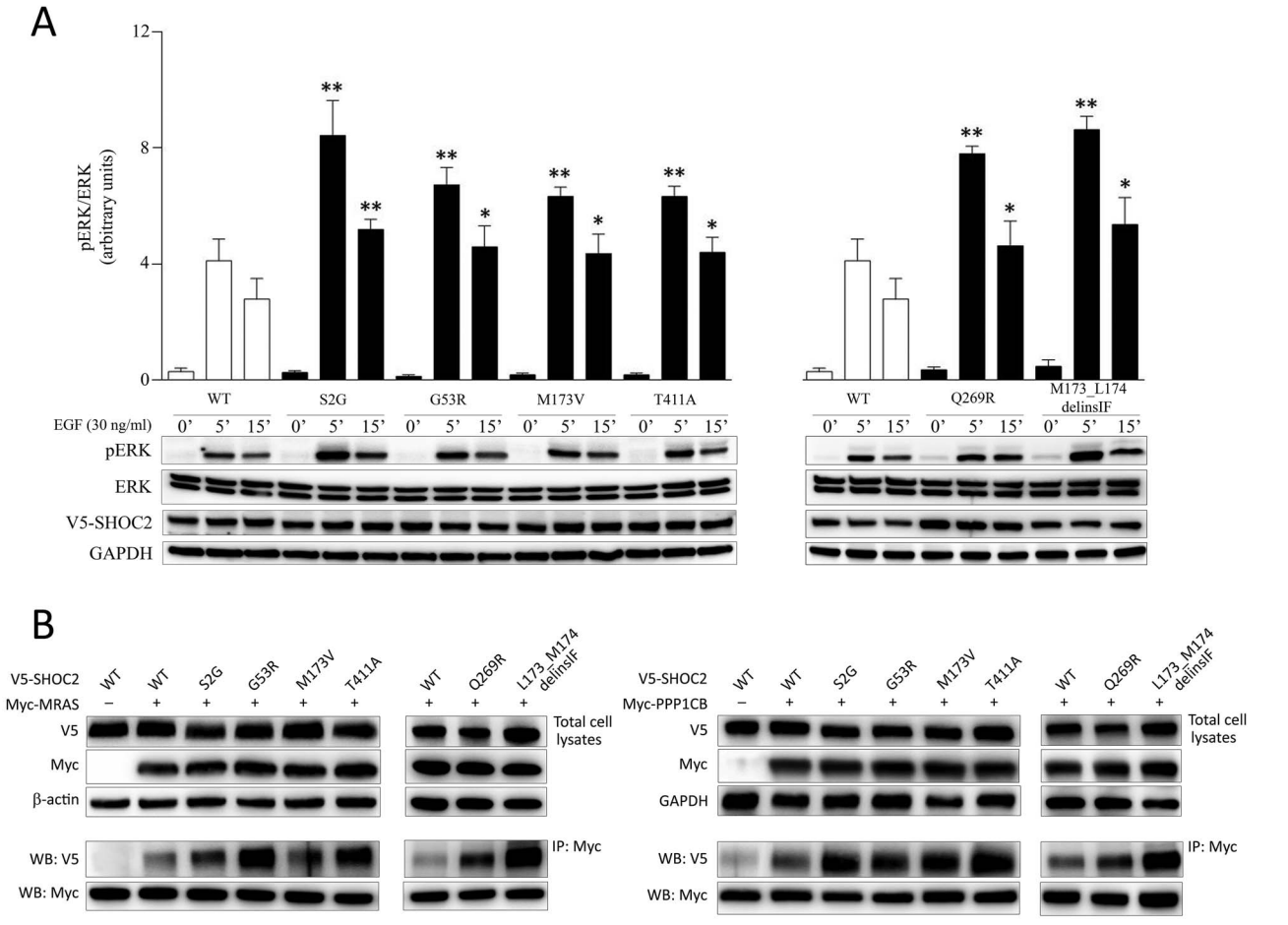


Figure 3. The pathogenic *SHOC2* variants promote increased stimulus-dependent MAPK signaling and enhance binding of SHOC2 to MRAS and PPP1CB. (**A**) Overexpression of SHOC2 mutants promoted variably enhanced ERK phosphorylation, as assessed by time-course experiments. Representative blots (below) and mean ± SD densitometry values (above) of two independent experiments are shown. Neuro2A cells were transiently transfected with the V5-tagged SHOC2 constructs, serum starved and treated with 30 ng/ml EGF for 5 or 15 min or left unstimulated. Equal amounts of cell lysates were resolved on 10% polyacrylamide gel. Asterisks indicate statistically significant differences compared to wild-type SHOC2 at the corresponding time upon EGF stimulation (∗indicates $P < 0.05$; ∗∗indicates $P < 0.005$; Two-way ANOVA followed by Tukey's multiple comparison test). (**B**) Enhanced binding of the SHOC2 mutants to MRAS and PPP1CB. Lysates from Neuro2A cells transiently transfected to express WT and V5-tagged SHOC2 mutant proteins with Myc-MRAS (left panel) or Myc-PPP1CB (right panel) were immunoprecipitated with an anti-Myc antibody and assayed by western blotting using the indicated antibodies.

and extension cell movements) and later in development (cardiac looping defects), which have been shown to be linked directly to enhanced MAPK signaling.

Discussion

Originally recognized in 2003, Mazzanti syndrome is an autosomal dominant RASopathy resembling NS, but having a distinctive constellation of ectodermal features involving skin and hair, and cardiac defects. This disorder is caused by a unique missense change in *SHOC2* (p.Ser2Gly) in most cases. Here, we functionally characterized five pathogenic *SHOC2* variants, four of which had not previously been reported, and used publicly available and new data to more accurately profile the clinical phenotype of this disorder. Finally, we established a GoF mechanism for all these pathogenic variants resulting in an enhanced signaling through the MAPK cascade.

SHOC2 is characterized by an unstructured *N*-terminal region (residues 2–101), followed by 20 LRRs (residues 102–564) and a short *C*-terminal tail (15). In the context of MAPK signaling, the unstructured *N*-terminal domain has been reported to mediate binding to MRAS (3) and HRAS (23), while the *C*-terminal portion of the first LRR subdomain is supposed to mediate the interaction with the catalytic PP1 subunit (24). Two LoF amino acid substitutions in Sur-8/Soc-2, the *Caenorhabditis elegans* ortholog, involving residues Asp^{220} and Glu^{502} (corresponding to Asp^{175} and Glu^{457} within LRR4 and LRR16 in SHOC2, respectively) were indeed documented to perturb the SHOC2-MRAS-PP1C complex formation (7,25). Besides the common p.Ser2Gly change, only two germline RASopathy-causing *SHOC2* variants, p.Met173Ile (LRR4) and Gln269_His270delinsHisTyr (LRR8), had been reported before this work (11,12), with conflicting interpretation of their functional impact on MAPK signaling. Our data provide evidence that the

Downloaded from https://academic.oup.com/hmg/advance-article/doi/10.1093/hmg/ddac071/6553889 by Koc University user on 27 April 2022

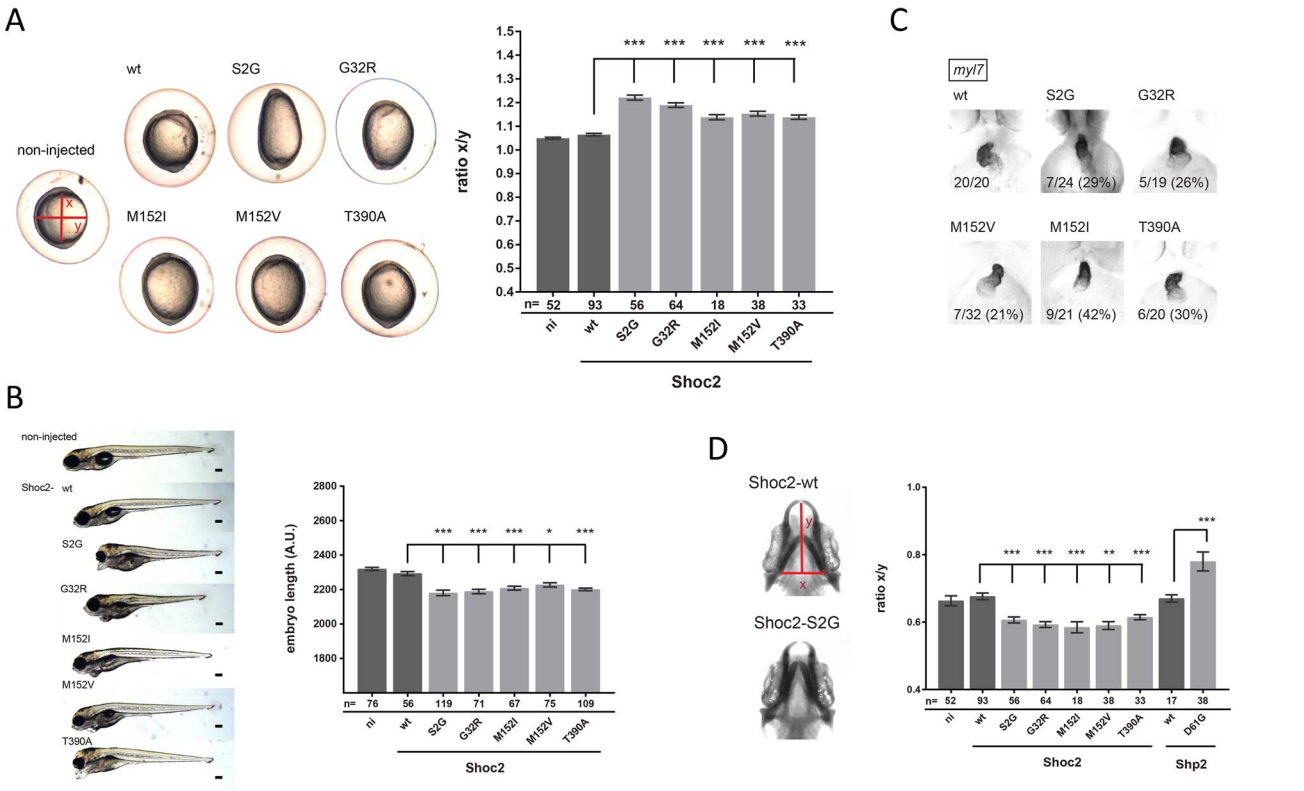


Figure 4. Developmental defects in zebrafish embryos expressing the Mazzanti syndrome-associated Shoc2 mutants. In all experiments, embryos were injected at the one-cell stage with mRNA encoding Shoc2 WT or Mazzanti syndrome-associated variants, or were not injected (ni) as a control. (**A**) Expression of the Shoc2 mutants induces epiboly defects. At 11 hpf, the embryos were imaged to assess ovality. Representative examples of non-injected and injected embryos are depicted (left). The ratio of the long (*x*) and short (*y*) axes is plotted (right). The number (*n*) of embryos that were analyzed is indicated. Tukey's honest significant difference test was done to assess significance. ***indicates $P < 0.001$. (**B**) Representative images of injected embryos at 5 dpf. Scale bar is 0.2 mm (left). The length of the body axis was determined for each embryo from the tip of the nose till the tip of the tail. Average lengths are plotted with the number (*n*) of embryos indicated (right). Tukey's honest significant difference test was done to assess significance. *indicates $P < 0.05$; **indicates $P < 0.01$; ***indicates $P < 0.001$. (**C**) Expression of Shoc2 mutants induced heart looping defects. At 3 dpf, embryos injected with synthetic mRNA as indicated were fixed and processed for *in situ* hybridization, using a cardiomyocyte-specific probe, *myl7*. Embryos were imaged from the ventral side, anterior to the top, illustrating characteristic looping of the heart in WT Shoc2 expressing embryos, as observed in non-injected controls (not shown). Aberrant non-looping phenotypes were observed in embryos expressing each of the SHOC2 mutants. The number of embryos showing aberrant looping over the total is indicated, as well as the percentage. (**D**) Embryos expressing the Shoc2 mutants show a reduction of the ceratohyal angle compared to non-injected embryos, or embryos expressing WT Shoc2, WT Shp2 or an NS-associated Shp2 (D61G) mutant. Embryos were fixed at 4 dpf and to image craniofacial defects, the cartilage was stained using Alcian blue. Stained embryos were imaged dorsally. The width of the ceratohyal (*x*) was determined as well as the distance to the tip of Meckel's cartilage (*y*). The *x*/*y* ratio directly represents quantitative craniofacial defects. Note that *Shoc2* KO embryos are characterized by an increase in the angle of the ceratohyal (28), whereas a decrease in this angle is observed in embryos expressing Shoc2 mutants, further supporting GoF. The averages of the *x*/*y* ratios are plotted. The number (*n*) of embryos that were analyzed is indicated. Tukey's honest significant difference test was done to assess significance. **indicates $P < 0.01$; ***indicates $P < 0.001$.

newly identified pathogenic variants do not significantly impact protein stability and subcellular localization, whereas they all enhance SHOC2 binding to both MRAS and PPP1CB, and promote increased EGF-stimulated MAPK signaling, in line with previously published findings (7,12). Besides confirming the functional relevance of residues Gly^{173} and Gln^{269}, the present results also document that missense substitutions affecting the unstructured *N*-terminal portion of the protein and other LRR motifs may cause GoF, indicating a complex organization of the protein in terms of functional interactions. Of note, while our *in vivo* data provided evidence for developmental defects in line with those that have previously been associated with upregulated MAPK signaling (22), expression of the pathogenic *Shoc2* variants in zebrafish embryos induced hypotelorism, which differs from what has been observed in embryos expressing the NS-associated Shp2 p.Asp61Gly variant (20). This phenotype is suggestive of the RhoA-signaling dependent phenotypes observed in *Wnt11* and *Fyn/Yes* knock-down zebrafish embryos (26). Since the postulated contribution of SHOC2 to other signaling circuits (27,28), and the relevance of RHO/CDC42/RAC signaling in developmental processes affected in RASopathies (29), this finding suggests that SHOC2's function may converge on RHO signaling to regulate neural crest cell migration.

Mazzanti syndrome is a phenotypically quite homogeneous disorder, which has been ascribed to the homogeneous genetic cause underlying this condition. The clinical presentation of the present subjects carrying new pathogenic *SHOC2* variants largely overlapped with that of previously reported individuals heterozygous for the

Downloaded from https://academic.oup.com/hmg/advance-article/doi/10.1093/hmg/ddac071/6553889 by Koc University user on 27 April 2022

p.Ser2Gly change. Cardiac involvement appeared however less pronounced, while left side anomalies seemed more frequent. Finally, short stature was less prevalent. It was previously suggested that pathogenic variants other than p.Ser2Gly might result in a milder phenotype (11). While the possibility that *SHOC2* variants with mild activating consequences on protein function might result in a mitigated RASopathy phenotype, the present findings do not support this hypothesis as a general rule.

Mazzanti syndrome has commonly been labeled as having a facies resembling NS; nonetheless, a systematic assessment of the major facial features characterizing this RASopathy had not previously been performed. Using the present and previously published series, we reviewed the clinical pictures of subjects with pathogenic *SHOC2* variants to comprehensively profile the disorder. Besides the striking occurrence of the majority of NS cardinal facial features (i.e. high forehead, hypertelorism, long and downslanted palpebral fissures, ptosis, low-set and posteriorly rotated ears, short neck with low posterior hairline), some of which had also been described in Mazzanti syndrome (1), other signs identified herein characterize the facial *gestalt* of the disorder, including short and triangular nose with anteverted nares (rarely reported in NS), deep and broad philtrum and peculiar upper lip conformation defined as 'exaggerated cupid bow'. The present review also revealed broad and laterally sparse eyebrows as a distinctive, recurrent ectodermal sign in the *SHOC2* cohort and identified it as a facial hallmark of Mazzanti syndrome. The critical comparison of the *SHOC2* cohort with the *PPP1CB* one also documented a similar occurrence of main signs/features, with a significantly less frequent occurrence of the philtrum- and upper lip-related signs in the subjects carrying pathogenic *PP1CB* variants.

A major challenge in using massive parallel sequencing in the routine diagnostics setting is linked to the interpretation of rare VoUS. The present report further emphasizes the current need of functional validation approaches directed to assess the clinical relevance of unclassified variants, and exemplifies the importance of integrating functional data in VoUS classification.

Materials and Methods

Study cohort

The six affected individuals recruited in the study were identified through routine molecular testing to confirm a clinical diagnosis of RASopathy (subjects 1–5) or in the frame of a research program dedicated to RASopathies (subject 6). For each subject, the phenotypic information was obtained through the referring clinician using a dedicated clinical questionnaire after signed informed consents were secured. Ethical approvals for this study were obtained from the Ethics Boards of the participating institutions (prot. 2013_OPBG_2020, Ospedale Pediatrico Bambino Gesù, Rome; prot. 06/19, Otto von Guericke University, Magdeburg; prot. 2020-002, Hôpital Robert Debré, Paris). Written informed consents were obtained from all the participating families. Explicit permission was obtained to publish the photographs shown in Figure 1A.

Genetic analyses

DNA was extracted from blood using standard techniques and subjected to exome sequencing (subject 6, Ospedale Pediatrico Bambino Gesù, Rome, Italy), Sanger sequencing (subject 2, Magdeburg University Hospital, Magdeburg, Germany) or parallel sequencing using a shared up-to-date RASopathy gene panel (subjects 1, 3–5; Robert Debré University Hospital, Paris, France; Magdeburg University Hospital). Exome sequencing (trio-based approach) was performed using the SureSelect Clinical Research Exome v2 and SureSelect Exome v7 (Agilent, Santa Clara, CA, USA) for target enrichment and a NovaSeq 6000 platform (Illumina, San Diego, CA, USA). WES data processing, including reads alignment (GRCh37/hg19 genome assembly), and variant filtering and prioritization by allele frequency, predicted functional impact, and inheritance were performed as previously reported (30–33). WES statistics and data output are reported in Supplementary Material, Table S2. Parallel sequencing used an up-to-date RASopathy gene panel including *BRAF*, *CBL*, *HRAS*, *KRAS*, *LZTR1*, *MAP2K1*, *MAP2K2*, *MRAS*, *NF1*, *NRAS*, *PPP1CB*, *PTPN11*, *RAF1*, *RRAS*, *RRAS2*, *RIT1*, *SHOC2*, *SOS1*, *SOS2*, *SPRED1* and *SPRED2*. Mutation scan was based on the use of a Nextera Rapid Capture Custom Enrichment kit (Illumina) (Magdeburg) or SureSelectQXT target enrichment system (Agilent) (Paris). Alignment and variant calling were performed with the MiSeq Reporter software (Illumina), followed by annotation of VCF output files using Variant Studio v.2.2 (Illumina) (Magdeburg), or using BenchlabNGS Alissa Interpret v.5.2 (Agilent) (Paris). All reported variants were visualized with the Integrative Genomics Viewer v.2.3 or Alamut Visual v.2.15 software. The identified *SHOC2* variants were deposited in ClinVar.

Structural analyses and molecular dynamics simulations

The starting model of WT SHOC2 was obtained from the AlphaFold database (UniProtKB: AF-Q1L8Y7-F1) (34). The unstructured N-terminal region of the model was not considered for the structural analyses. The stability of the starting structure was validated by molecular dynamics (MD) simulation by simulating up to 500 ns. Each amino acid substitution was introduced in a stabilized snapshot (after ~100 ns of MD simulation) using the UCSF Chimera package (35). The side-chain orientations were obtained with the Dunbrack backbone-dependent rotamer library (36), choosing in all cases the best rotamer that had the least/no steric clashes with the neighboring residues. The starting structures were embedded in a cubic box, extending up to 18 Å from the solute, and immersed in TIP3P water molecules (37). Counter ions were added to neutralize the overall charge with the genion gromacs tool. After energy

Downloaded from https://academic.oup.com/hmg/advance-article/doi/10.1093/hmg/ddac071/6553889 by Koc University user on 27 April 2022

minimizations, the systems were slowly relaxed for 5 ns by applying positional restraints of 1000 kJ mol-1 nm-2 to the protein atoms. The unrestrained MD simulations were carried out for a length of 500 ns with a time step of 2 fs with the Gromacs v.2020 package (38) and the amber ff14SB force field (39). V-rescale temperature coupling was employed to keep the temperature constant at 300 K (40). The Particle-Mesh Ewald method was used for the treatment of the long-range electrostatic interactions (41). The first 50 ns portion of the trajectory was excluded from the analysis. All analyses were performed using the MDAnalysis package (42,43).

Functional validation analyses

Reagents

Dulbecco's modified Eagle's medium (DMEM), fetal bovine serum (FBS), phosphate-buffered saline, glutamine and antibiotics were obtained from Euroclone (Wetherby, UK). Fugene6 transfection reagent and complete protease inhibitor cocktail tablets were purchased from Roche Diagnostics (Mannheim, Germany). CHX and MG132 were from Sigma-Aldridge (St. Louis, MO, USA). Trans-Blot Turbo Transfer Packs were from Bio-Rad Laboratories (Hercules, CA, USA). ECL Western Blotting Detection reagents were obtained from Pierce Biotechnology (Rockford, IL, USA). QuiKChange II Site-Directed Mutagenesis kit was obtained from Stratagene (La Jolla, CA, USA). pcDNA6.2/V5-HisA eukaryotic expression vector and EGF were from Invitrogen (Carlsbad, CA, USA). Protein G Sepharose was obtained from GE Healthcare (Freiburg, Germany). The following antibodies were used: mouse monoclonal anti-V5 (Invitrogen); mouse monoclonal anti-Myc, rabbit polyclonal anti-Na/K-ATPase, rabbit polyclonal anti-p44/42 MAPK1/3, mouse monoclonal anti-phospho-p44/42 MAPK1/3 (Thr202/Tyr204 of Erk1 and Thr185/Tyr187 of Erk2) (Cell Signaling Technology, Danvers, MA, USA); mouse monoclonal anti-β-actin, mouse monoclonal anti-HSP90, horseradish peroxidase-conjugated anti-rabbit or anti-mouse (Sigma-Aldrich); mouse monoclonal anti-GAPDH, rabbit polyclonal anti-YY1 (Santa Cruz, Dallas, CA, USA); goat anti-mouse conjugated to Alexa Fluor 594 and Alexa Fluor 488 phalloidin dye were from Molecular Probes (Eugene, OR, USA). Vectashield antifade medium containing DAPI was purchased from Vector Laboratories (Burlingame, CA, USA). Phenylthiourea (PTU), Alcian blue and MS-222 were obtained from Sigma-Aldrich. mMESSAGE SP6 Transcription Kit was from TermoFisher Scientific (Waltham, MA, USA), while the Q5 Site-Directed Mutagenesis Kit was from New England Biolabs (Ipswich, MA, USA). The *myl7*-specific probe was previously described (22).

Constructs

The entire coding sequence of WT SHOC2 was cloned into the pcDNA6.2/V5-HisA eukaryotic expression vector. Mutant SHOC2 constructs carrying the p.Gly53Arg, p.Met173Val, p.Gln269Arg, p.Thr411Ala or p.Met173_Leu174delinsIlePhe amino acid substitutions were generated by PCR-based site-directed mutagenesis using the QuiKChange II Site-Directed Mutagenesis Kit (15). The identity of each construct was verified by bidirectional sequencing (ABI BigDye terminator Sequencing Kit v3.1, SeqStudio Genetic Analyzer; Applied Biosystems, Foster City, CA, USA). pcDNA3.1-Myc-MRAS and pcDNA3.1-Myc-PPP1CB constructs were produced as previously reported (12). pCR-Blunt II-TOPO vector was from TermoFisher Scientific.

Zebrafish Shoc2 was amplified from cDNA of 5 days old zebrafish embryos by nested PCR using the primers pair 5′-CGAACAAAATACAAGAGCGAGAG-3′ and 5′-GCCAATCTAGATCAGACCATGGC-3′ in the first reaction and primer pair 5′-GCGGATCCATGAGCAGTACTCTG-3′ and 5′-GCCAATCTAGATCAAGCGTAATCTGGAACATCGTATGGGTAGACCATGGCGCGGTAGGG-3′ in the second reaction. In the second reaction, the HA tag was added to the C-terminus of the construct. PCR product was cloned into the pCR-Blunt II-TOPO vector to generate pCR-Blunt II-TOPO-SHOC2-HA. From here SHOC2-HA was subcloned into the *BamHI* and *XbaI* restriction sites of pCS2+ vector to generate pCS2+ SHOC2-HA. pCS2+ SHOC2-HA plasmid served as template to introduce the missense changes resulting in the S2G, G32R, M152I, M152V and T390A amino acid substitutions, which correspond to the patient-associated S2G, G53R, M173I, M173V and T411A substitutions, respectively. S2G mutation was introduced by PCR using the primer pair 5′-GCGGATCCATGGGCAGTACTCTG-3′ and 5′-GCCAATCTAGATCAAGCGTAATCTGGAACATCGTATGGGTAGACCATGGCGCGGTAGGG-3′. Other mutations were introduced by Q5 Site-Directed Mutagenesis Kit. All constructs were verified by sequencing (Macrogen Europe B.V., Amsterdam, the Netherlands). mRNA used for injections of zebrafish embryos was produced from the pCS2+ SHOC2 constructs using the mMESSAGE mMACHINE SP6 Transcription Kit.

Cell culture, transfection, inhibitor treatment and EGF stimulation

COS-1 and Neuro2A cells were cultured in DMEM medium supplemented with 10% heat-inactivated FBS, 1% L-glutamine and antibiotics (37°C, humidified atmosphere containing 5% CO_2). Subconfluent cells were transfected using the Fugene6 transfection reagent, according to the manufacturer's instructions. Cells were treated with CHX (100 μg/ml) or MG132 (50 μM) to analyze protein stability and degradation. Serum-free DMEM and EGF (30 ng/ml) were utilized to starve and stimulate cells, respectively.

Cell homogenate, immunoblotting, cell fractionation and co-immunoprecipitation (co-IP) assays

Cells were lysed in radio-immune precipitation assay buffer, pH 8.0, supplemented with 20 mM NaF, 1 mM Na_3VO_4 and protease inhibitors. Lysates were centrifuged at 16 000 *g* for 20 min at 4°C, and supernatant protein

Downloaded from https://academic.oup.com/hmg/advance-article/doi/10.1093/hmg/ddac071/6553889 by Koc University user on 27 April 2022

concentration was determined by BCA assay (44), using BSA as standard. Western blotting (WB) and densitometric analyses were performed as previously described (15,30,33). Cell fractionation was performed as previously reported (15,33), using transfected COS-1 cells serum-starved overnight and then EGF-stimulated or left untreated. Each subcellular fraction was subjected to SDS-PAGE and WB to determine the SHOC2 distribution in the different cellular compartments. Membranes were probed with antibodies to HSP90 (cytoplasmic marker), YY1 (nuclear marker) and Na/K-ATPase (plasma membrane marker). SHOC2/MRAS and SHOC2/PPP1CB co-IP assays were performed on transfected Neuro2A cells serum starved for 16 h, and then stimulated with EGF, as reported (9,12,45).

Confocal laser scanning microscopy

COS-1 cells (15×10^3) were seeded on glass coverslips, transfected with the various constructs (24 h), serum starved (16 h) and stimulated with EGF (15 min) or left unstimulated. Cells were fixed with 4% paraformaldehyde (30 min, 4°C) and permeabilized (0.05% Triton X-100, 10 min, room temperature). Cells were then stained with a mouse monoclonal anti-V5 followed by goat anti-mouse Alexa Fluor 594, and then with Alexa Fluor 488 phalloidin dye. Finally, glass coverslips were mounted on microscope slides using Vectashield antifade medium containing DAPI, and analyzed using an Olympus FluoView FV1000 apparatus, utilizing excitation spectral laser lines at 405, 488 and 568 nm. Signals from different fluorescent probes were taken in sequential scanning mode.

Zebrafish husbandry

Experimental animal procedures were approved by the local animal experiments committee of the Royal Netherlands Academy of Arts and Sciences (KNAW), and performed following local guidelines and policies in agreement with national and European law. Maintenance of zebrafish was performed as described previously (46,47). PTU (0.003%, v/v) was added to the E3 medium at 24 hpf to block pigmentation.

Phenotypic assessment of zebrafish embryos

Zebrafish embryos were injected at the one-cell stage in the yolk with a mixture of 40 ng/μl mRNA encoding SHOC2 (WT or variant), and 50 ng/μl mRNA encoding GFP. GFP positive embryos were selected for phenotypic readouts. Images were collected using Leica M165 FC stereomicroscopes (Leica Biosystems, Wetzlar, Germany) and analyzed using ImageJ (U.S. National Institutes of Health, Bethesda, MD, USA). To determine epiboly defects, the ratio of the major (x) and minor (y) axis was determined in 11 hpf embryos. Lengths of 3 and 5 dpf anesthetized (0.1% MS-222) embryos were determined by lateral imaging. *In situ* hybridization was performed as described using *myl7*-specific probe in PTU-treated 3 dpf embryos (22). Alcian blue staining of the cartilage in PTU-treated 4 dpf embryos was performed as described (48). The ratio between the width of the head (x) and the distance from the back of the head to Meckel's cartilage (y) was determined.

Statistical analysis was performed using GraphPad Prism 7.05 (GraphPad Software Inc., San Diego, CA, USA) using the analysis of variance complemented by Tukey's honest significant difference test.

Supplementary Material

Supplementary Material is available at *HMG* online.

Conflict of Interest statement. The authors declare that they do not have any conflict of interest.

Funding

The authors thank the subjects and their families for participating in this study, and Bruno Leheup (University Hospital of Nancy, Nancy, France) for clinical support; European Joint Program on Rare Diseases (EJP-RD) (NSEuroNet, to H.C., M.Z., J.dH. and M.T.); Associazione Italiana per la Ricerca sul Cancro (AIRC) (IG 21614, to M.T.); Italian Ministry of Health (Ricerca Corrente 2022, to M.M. and M.T.; CCR-2017-23669081 and RCR-2020-23670068_001, to M.T.; FR-2018-12366931 to G.C.); Italian Ministry of Research (FOE 2019, to M.T.); German Federal Ministry of Education and Research—BMBF (German Network for RASopathy Research 'GeNeRARe', FKZ: 01GM1902A to M.Z). This work has been carried out in the frame of the European Reference Network on Rare Congenital Malformations and Rare Intellectual Disability (ERN-ITHACA) activity.

References

1. Mazzanti, L., Cacciari, E., Cicognani, A., Bergamaschi, R., Scarano, E. and Forabosco, A. (2003) Noonan-like syndrome with loose anagen hair: a new syndrome? *Am. J. Med. Genet. A*, **118A**, 279–286.
2. Cordeddu, V., Di Schiavi, E., Pennacchio, L.A., Ma'ayan, A., Sarkozy, A., Fodale, V., Cecchetti, S., Cardinale, A., Martin, J., Schackwitz, W. *et al.* (2009) Mutation of SHOC2 promotes aberrant protein *N*-myristoylation and causes Noonan-like syndrome with loose anagen hair. *Nat. Genet.*, **41**, 1022–1026.
3. Rodriguez-Viciana, P., Oses-Prieto, J., Burlingame, A., Fried, M. and McCormick, F. (2006) A phosphatase holoenzyme comprised of Shoc2/Sur8 and the catalytic subunit of PP1 functions as an M-Ras effector to modulate Raf activity. *Mol. Cell*, **22**, 217–230.
4. Kwon, J.J. and Hahn, W.C. (2021) A leucine-rich repeat protein provides a SHOC2 the RAS circuit: a structure-function perspective. *Mol. Cell. Biol.*, **41**, e00627–e00620.
5. Gripp, K.W., Aldinger, K.A., Bennett, J.T., Baker, L., Tusi, J., Powell-Hamilton, N., Stabley, D., Sol-Church, K., Timms, A.E. and Dobyns, W.B. (2016) A novel rasopathy caused by recurrent de novo missense mutations in PPP1CB closely resembles Noonan syndrome with loose anagen hair. *Am. J. Med. Genet. A*, **170**, 2237–2247.

Downloaded from https://academic.oup.com/hmg/advance-article/doi/10.1093/hmg/ddac071/6553889 by Koc University user on 27 April 2022

6. Ma, L., Bayram, Y., McLaughlin, H.M., Cho, M.T., Krokosky, A., Turner, C.E., Lindstrom, K., Bupp, C.P., Mayberry, K., Mu, W. *et al.* (2016) De novo missense variants in PPP1CB are associated with intellectual disability and congenital heart disease. *Hum. Genet.*, **135**, 1399–1409.
7. Young, L.C., Hartig, N., Boned Del Río, I., Sari, S., Ringham-Terry, B., Wainwright, J.R., Jones, G.G., McCormick, F. and Rodriguez-Viciana, P. (2018) SHOC2-MRAS-PP1 complex positively regulates RAF activity and contributes to Noonan syndrome pathogenesis. *Proc. Natl. Acad. Sci. U. S. A.*, **115**, E10576–E10585.
8. Higgins, E.M., Bos, J.M., Mason-Suares, H., Tester, D.J., Ackerman, J.P., MacRae, C.A., Sol-Church, K., Gripp, K.W., Urrutia, R. and Ackerman, M.J. (2017) Elucidation of MRAS-mediated Noonan syndrome with cardiac hypertrophy. *JCI Insight.*, **2**, e91225.
9. Motta, M., Sagi-Dain, L., Krumbach, O.H.F., Hahn, A., Peleg, A., German, A., Lissewski, C., Coppola, S., Pantaleoni, F., Kocherscheid, L. *et al.* (2020) Activating MRAS mutations cause Noonan syndrome associated with hypertrophic cardiomyopathy. *Hum. Mol. Genet.*, **29**, 1772–1783.
10. Gripp, K.W., Zand, D.J., Demmer, L., Anderson, C.E., Dobyns, W.B., Zackai, E.H., Denenberg, E., Jenny, K., Stabley, D.L. and Sol-Church, K. (2013) Expanding the SHOC2 mutation associated phenotype of Noonan syndrome with loose anagen hair: structural brain anomalies and myelofibrosis. *Am. J. Med. Genet. A*, **161A**, 2420–2430.
11. Hannig, V., Jeoung, M., Jang, E.R., Phillips, J.A., 3rd and Galperin, E. (2014) A novel SHOC2 variant in Rasopathy. *Hum. Mutat.*, **35**, 1290–1294.
12. Motta, M., Giancotti, A., Mastromoro, G., Chandramouli, B., Pinna, V., Pantaleoni, F., Di Giosaffatte, N., Petrini, S., Mazza, T., D'Ambrosio, V. *et al.* (2019) Clinical and functional characterization of a novel RASopathy-causing SHOC2 mutation associated with prenatal-onset hypertrophic cardiomyopathy. *Hum. Mutat.*, **40**, 1046–1056.
13. Boned Del Río, I., Young, L.C., Sari, S., Jones, G.G., Ringham-Terry, B., Hartig, N., Rejnowicz, E., Lei, W., Bhamra, A., Surinova, S. *et al.* (2019) SHOC2 complex-driven RAF dimerization selectively contributes to ERK pathway dynamics. *Proc. Natl. Acad. Sci. U. S. A.*, **116**, 13330–13339.
14. Komatsuzaki, S., Aoki, Y., Niihori, T., Okamoto, N., Hennekam, R.C., Hopman, S., Ohashi, H., Mizuno, S., Watanabe, Y., Kamasaki, H. *et al.* (2010) Mutation analysis of the SHOC2 gene in Noonan-like syndrome and in hematologic malignancies. *J. Hum. Genet.*, **55**, 801–809.
15. Motta, M., Chillemi, G., Fodale, V., Cecchetti, S., Coppola, S., Stipo, S., Cordeddu, V., Macioce, P., Gelb, B.D. and Tartaglia, M. (2016) SHOC2 subcellular shuttling requires the KEKE motif-rich region and N-terminal leucine-rich repeat domain and impacts on ERK signalling. *Hum. Mol. Genet.*, **2**, 3824–3835.
16. Enkhbayar, P., Kamiya, M., Osaki, M., Matsumoto, T. and Matsushima, N. (2004) Structural principles of leucine-rich repeat (LRR) proteins. *Proteins*, **54**, 394–403.
17. Li, W., Han, M. and Guan, K.L. (2000) The leucine-rich repeat protein SUR8 enhances MAP kinase activation and forms a complex with Ras and Raf. *Genes Dev.*, **14**, 895–900.
18. Matsunaga-Udagawa, R., Fujita, Y., Yoshiki, S., Terai, K., Kamioka, Y., Kiyokawa, E., Yugi, K., Aoki, K. and Matsuda, M. (2010) The scaffold protein Shoc2/SUR-8 accelerates the interaction of Ras and Raf. *J. Biol. Chem.*, **285**, 7818–7826.
19. Jang, H., Oakley, E., Forbes-Osborne, M., Kesler, M.V., Norcross, R., Morris, A.C. and Galperin, E. (2019) Hematopoietic and neural crest defects in zebrafish shoc2 mutants: a novel vertebrate model for Noonan-like syndrome. *Hum. Mol. Genet.*, **28**, 501–514.
20. Jopling, C., Van Geemen, D. and Den Hertog, J. (2007) Shp2 knockdown and noonan/LEOPARD mutant Shp2-induced gastrulation defects. *PLoS Genet.*, **3**, e225.
21. Jindal, G.A., Goyal, Y., Yamaya, K., Futran, A.S., Kountouridis, I., Balgobin, C.A., Schüpbach, T., Burdine, R.D. and Shvartsman, S.Y. (2016) *In vivo* severity ranking of mutations associated with RASopathies. *Proc. Natl. Acad. Sci. U. S. A.*, **114**, 510–515.
22. Bonetti, M., Paardekooper, O.J., Tessadori, F., Noël, E., Bakkers, J. and Den Hertog, J. (2014) Noonan and LEOPARD syndrome Shp2 variants induce heart displacement defects in zebrafish. *Development*, **141**, 1961–1970.
23. Sieburth, D.S., Sun, Q. and Han, M. (1998) SUR-8, a conserved Ras-binding protein with leucine-rich repeats, positively regulates Ras-mediated signaling in *C. elegans*. *Cell*, **94**, 119–130.
24. Young, L.C., Hartig, N., Muñoz-Alegre, M., Oses-Prieto, J.A., Durdu, S., Bender, S., Vijayakumar, V., Vietri Rudan, M., Gewinner, C., Henderson, S. *et al.* (2013) An MRAS, SHOC2, and SCRIB complex coordinates ERK pathway activation with polarity and tumorigenic growth. *Mol. Cell*, **52**, 679–692.
25. Kota, P., Terrell, E.M., Ritt, D.A., Insinna, C., Westlake, C.J. and Morrison, D.K. (2019) M-Ras/Shoc2 signaling modulates E-cadherin turnover and cell-cell adhesion during collective cell migration. *Proc. Natl. Acad. Sci. U. S. A.*, **116**, 3536–3545.
26. Jopling, C. and Den Hertog, J. (2005) Fyn/Yes and non-canonical Wnt signalling converge on RhoA in vertebrate gastrulation cell movements. *EMBO Rep.*, **6**, 426–431.
27. Dai, P., Xiong, W.C. and Mei, L. (2006) Erbin inhibits RAF activation by disrupting the sur-8-Ras-Raf complex. *J. Biol. Chem.*, **281**, 927–933.
28. Xie, C.M., Tan, M., Lin, X.T., Wu, D., Jiang, Y., Tan, Y., Li, H., Ma, Y., Xiong, X. and Sun, Y. (2019) The FBXW7-SHOC2-Raptor Axis Controls the Cross-Talks between the RAS-ERK and mTORC1 Signaling Pathways. *Cell Rep.*, **26**, 3037–3050.e4.
29. Martinelli, S., Krumbach, O.H.F., Pantaleoni, F., Coppola, S., Amin, E., Pannone, L., Nouri, K., Farina, L., Dvorsky, R. and Lepri, F. (2018) Functional dysregulation of CDC42 causes diverse developmental phenotypes. *Am. J. Hum. Genet.*, **102**, 309–320.
30. Motta, M., Pannone, L., Pantaleoni, F., Bocchinfuso, G., Radio, F.C., Cecchetti, S., Ciolfi, A., Di Rocco, M., Elting, M.W., Brilstra, E.H. *et al.* (2020) Enhanced MAPK1 function causes a neurodevelopmental disorder within the RASopathy clinical spectrum. *Am. J. Hum. Genet.*, **107**, 499–513.
31. Radio, F.C., Pang, K., Ciolfi, A., Levy, M.A., Hernández-García, A., Pedace, L., Pantaleoni, F., Liu, Z., de Boer, E., Jackson, A. *et al.* (2021) SPEN haploinsufficiency causes a neurodevelopmental disorder overlapping proximal 1p36 deletion syndrome with an episignature of X chromosomes in females. *Am. J. Hum. Genet.*, **108**, 502–516.
32. Lin, Y.C., Niceta, M., Muto, V., Vona, B., Pagnamenta, A.T., Maroofian, R., Beetz, C., van Duyvenvoorde, H., Dentici, M.L., Lauffer, P. *et al.* (2021) SCUBE3 loss-of-function causes a recognizable recessive developmental disorder due to defective bone morphogenetic protein signaling. *Am. J. Hum. Genet.*, **108**, 115–133.
33. Motta, M., Fasano, G., Gredy, S., Brinkmann, J., Bonnard, A.A., Simsek-Kiper, P.O., Gulec, E.Y., Essaddam, L., Utine, G.E., Guarnetti Prandi, I. *et al.* (2021) SPRED2 loss-of-function causes a recessive Noonan syndrome-like phenotype. *Am. J. Hum. Genet.*, **108**, 2112–2129.
34. Jumper, J., Evans, R., Pritzel, A., Green, T., Figurnov, M., Ronneberger, O., Tunyasuvunakool, K., Bates, R., Žídek, A., Potapenko, A. *et al.* (2021) Highly accurate protein structure prediction with AlphaFold. *Nature*, **596**, 583–589.

Downloaded from https://academic.oup.com/hmg/advance-article/doi/10.1093/hmg/ddac071/6553889 by Koc University user on 27 April 2022

35. Pettersen, E.F., Goddard, T.D., Huang, C.C., Couch, G.S., Greenblatt, D.M., Meng, E.C. and Ferrin, T.E. (2004) UCSF Chimera–a visualization system for exploratory research and analysis. *J. Comput. Chem.*, **25**, 1605–1612.
36. Dunbrack, R.L., Jr. (2002) Rotamer libraries in the 21st century. *Curr. Opin. Struct. Biol.*, **12**, 431–440.
37. Jorgensen, W.L., Chandrasekhar, J., Madura, J.D., Impey, R.W. and Klein, M.L. (1983) Comparison of simple potential functions for simulating liquid water. *J. Chem. Phys.*, **79**, 926.
38. Pronk, S., Pàll, S., Schulz, R., Larsson, P., Bjelkmar, P., Apostolov, R., Shirts, M.R., Smith, J.C., Kasson, P.M., van der Spoel, D. *et al.* (2013) GROMACS 4.5: a high-throughput and highly parallel open source molecular simulation toolkit. *Bioinformatics*, **29**, 845–854.
39. Hornak, V., Abel, R., Okur, A., Strockbine, B., Roitberg, A. and Simmerling, C. (2006) Comparison of multiple Amber force fields and development of improved protein backbone parameters. *Proteins*, **5**, 712–725.
40. Bussi, G., Donadio, D. and Parrinello, M. (2007) Canonical sampling through velocity rescaling. *J. Chem. Phys.*, **126**, 014101.
41. Darden, T., York, D. and Pedersen, L. (1993) Particle mesh Ewald: An N log(N) method for Ewald sums in large systems. *J. Chem. Phys.*, **98**, 10089.
42. Michaud-Agrawal, N., Denning, E.J., Woolf, T.B. and Beckstein, O. (2011) MDAnalysis: a toolkit for the analysis of molecular dynamics simulations. *J. Comput. Chem.*, **32**, 2319–2327.
43. Gowers, R.J., Linke, M., Barnoud, J., Reddy, T.H.E., Melo, M.N., Seyler, S.L., Domanski, J., Dotson, D.L., Buchoux, S., Kenney, I.M., *et al.* (2016) MDAnalysis: a Python package for the rapid analysis of molecular dynamics simulations. In Benthall, S. and Rostrup, S. (eds), *Proceedings of the 15th Python in Science Conference*, Austin, Texas. pp. 98–105.
44. Smith, P.K., Krohn, R.I., Hermanson, G.T., Mallia, A.K., Gartner, F.H., Provenzano, M.D., Fujimoto, E.K., Goeke, N.M., Olson, B.J. and Klenk, D.C. (1985) Measurement of protein using bicinchoninic acid. *Anal. Biochem.*, **150**, 76–85.
45. Kaboord, B. and Perr, M. (2008) Isolation of proteins and protein complexes by immunoprecipitation. *Methods Mol. Biol.*, **424**, 349–364.
46. Aleström, P., D'Angelo, L., Midtlyng, P.J., Schorderet, D.F., Schulte-Merker, S., Sohm, F. and Warner, S. (2020) Zebrafish: housing and husbandry recommendations. *Lab. Anim.*, **54**, 213–224.
47. Whitlock, K.E. and Westerfield, M. (2000) The olfactory placodes of the zebrafish form by convergence of cellular fields at the edge of the neural plate. *Development*, **127**, 3645–3653.
48. Paardekooper Overman, J., Preisinger, C., Prummel, K., Bonetti, M., Giansanti, P., Heck, A. and den Hertog, J. (2014) Phosphoproteomics-mediated identification of Fer kinase as a target of mutant Shp2 in Noonan and LEOPARD syndrome. *PLoS One*, **9**, e106682.

Downloaded from https://academic.oup.com/hmg/advance-article/doi/10.1093/hmg/ddac071/6553889 by Koc University user on 27 April 2022